JGR Atmospheres

RESEARCH ARTICLE
10.1029/2019JD031017

Quantifying the Drivers of the Clear Sky Greenhouse Effect, 2000–2016

Shiv Priyam Raghuraman[1], **David Paynter**[2], **and V. Ramaswamy**[2]

[1]Program in Atmospheric and Oceanic Sciences, Princeton University, Princeton, NJ, USA, [2]Geophysical Fluid Dynamics Laboratory, NOAA, Princeton, NJ, USA

Key Points:
- Global mean clear sky greenhouse effect (G) over 2000–2016 is 130–133 W m^{-2} and its sensitivity to surface temperature is 3.1–4.0 W m^{-2} K^{-1}
- Middle and upper tropospheric water vapor contribute equally to anomalies in global G, while regionally midtroposphere dominates
- Variations in relative humidity are crucial in explaining regional anomalies in G and help generate the clear sky super greenhouse effect

Supporting Information:
- Supporting Information S1
- Figure S1
- Figure S2
- Figure S3
- Figure S4
- Figure S5
- Figure S6
- Figure S7

Correspondence to:
S. P. Raghuraman,
shivr@princeton.edu

Citation:
Raghuraman, S. P., Paynter, D., & Ramaswamy, V. (2019). Quantifying the drivers of the clear sky greenhouse effect, 2000–2016. *Journal of Geophysical Research: Atmospheres*, *124*, 11,354–11,371. https://doi.org/10.1029/2019JD031017

Received 17 MAY 2019
Accepted 5 OCT 2019
Accepted article online 2 NOV 2019
Published online 15 NOV 2019

Abstract The clear sky greenhouse effect (G) is defined as the trapping of infrared radiation by the atmosphere in the absence of clouds. The magnitude and variability of G is an important element in the understanding of Earth's energy balance; yet the quantification of the governing factors of G is poor. The global mean G averaged over 2000 to 2016 is 130–133 W m^{-2} across data sets. We use satellite observations from Clouds and the Earth's Radiant Energy System Energy Balance and Filled (CERES EBAF) to calculate the monthly anomalies in the clear sky greenhouse effect (ΔG). We quantify the contributions to ΔG due to changes in surface temperature, atmospheric temperature, and water vapor by performing partial radiation perturbation experiments using ERA-Interim and Geophysical Fluid Dynamics Laboratory's Atmospheric Model 4.0 climatological data. Water vapor in the middle troposphere and upper troposphere is found to contribute equally to the global mean and tropical mean ΔG. Holding relative humidity (RH) fixed in the radiative transfer calculations captures the temporal variability of global mean ΔG while variations in RH control the regional ΔG signal. The variations in RH are found to help generate the clear sky super greenhouse effect (SGE). Thirty-six percent of Earth's area exhibits SGE, and this disproportionately contributes to 70% of the globally averaged magnitude of ΔG. In the global mean, G's sensitivity to surface temperature is 3.1–4.0 W m^{-2} K^{-1}, and the clear sky longwave feedback parameter is 1.5–2.0 W m^{-2} K^{-1}. Observations from CERES EBAF lie at the more sensitive ends of these ranges and the spread arises from its cloud removal treatment, suggesting that it is difficult to constrain clear sky feedbacks.

1. Introduction

The clear sky greenhouse effect (G) is known to maintain Earth's temperature at habitable levels but has been perturbed by natural variability and anthropogenic influences over the past century with significant implications for the climate system. It can be measured by the difference between the surface upwelling flux (E) and the clear sky outgoing longwave radiation (OLR) at the top of the atmosphere,

$$G = E - \mathrm{OLR} \approx \sigma T_s^4 - \mathrm{OLR}. \quad (1)$$

Since March 2000, there has been a continuous time series of G from the Clouds and the Earth's Radiant Energy System Energy Balance and Filled (CERES EBAF) observational data set. The goal of this study is to use this observational data set to characterize how G varied during this time period and breakdown the factors responsible for G's temporal anomalies by carrying out partial radiation perturbation experiments.

Previous studies that aimed to explain the physics of the greenhouse effect used only a few discontinuous months of Earth's Radiation Budget Experiment (ERBE) (Raval & Ramanathan, 1989) data, ship data and radiosondes. Moreover, they correlated G and SST for all points around the Earth and obtained linear fits that were not representative of the physics of a given region (Hallberg & Inamdar, 1993; Inamdar & Ramanathan, 1994; 1998; Soden & Fu, 1995; Raval & Ramanathan, 1989). Studies which carried out sensitivity analyses of G only used one month of data and relied on fixed perturbations (Huang et al., 2007 and Dessler et al., 2008) which are not representative of observed anomalies, i.e., deviations from a climatology. A breakdown with only one month does not allow us to deduce what factors are responsible for the transition from negative to positive anomalies for any given location. Studies that had a longer time series did not attempt to explain the drivers of the anomalies and only showed a comparison between observations and general circulation models (Soden, 1997 and Radley et al., 2014).

Our paper builds on this past work by experimentally determining the causes of monthly anomalies in G. We use climatological data from European Centre for Medium Range Weather Forecasts (ECMWF) Re-Analysis-Interim (ERA-Interim) and Geophysical Fluid Dynamics Laboratory's (GFDL) Atmospheric Model (AM4) as input for a radiative transfer model to decompose the anomalies in G into contributions from surface temperature, atmospheric temperature, water vapor. Gambacorta et al. (2008) motivated readers to study how OLR (and hence G) depends on the water vapor vertical distribution, so we further decompose water vapor's contributions into the lower, middle, and upper troposphere. Globally averaged changes in top of atmosphere clear sky OLR follow the fixed relative humidity (RH) approximation over long time scales such as global warming (Manabe & Wetherald, 1967). However, whether ΔG follows the fixed RH approximation during interannual variability has not been studied in detail and hence is one of the key foci of our paper.

The time series spanning 16.5 years allows us to characterize the frequently occurring super greenhouse effect (SGE), the phenomenon in which the rate of change of G with surface temperature exceeds the surface emission's rate (Hallberg & Inamdar, 1993; Stephens et al., 2016; Valero et al., 1997). Hallberg and Inamdar (1993) focused on surface temperatures above 298 K, where G was found to nonlinearly increase. Recently, Koll and Cronin (2018) showed a nonlinear decrease in clear sky OLR at high temperatures, which can also be characterized as SGE. Past work on SGE has been based on idealized models that used a single global mean column and did not account for RH variations (Dewey & Goldblatt, 2018). It also did not focus on questions such as what percentage of Earth's area experiences SGE, how often does it occur across the globe, and what factors make a particular location transition from a regular greenhouse state to a super greenhouse state from 1 month to the next (Huang & Ramaswamy, 2008; Kahn et al., 2016; Stephens et al., 2016). Our paper seeks to address these outstanding questions about SGE in the current climate.

In the following section we describe the data and methods that we used. In section 3 we present our results starting with section 3.1 where we compare G of GFDL's AM4 to ERA-I and CERES data sets, which Held and Soden (2000) deemed important for testing the skill of general circulation models for future climate change predictions. In section 3.2, to explain the origins of ΔG every month, we decompose ΔG into its contributions from surface temperature, atmospheric temperature, and water vapor. We investigate whether fixed RH controls interannual variations in ΔG regionally and globally in section 3.3. In section 3.4, we examine how sensitive ΔG is to changes in surface temperature. We also estimate the clear sky longwave feedback parameter across different data sets to understand how sensitive the climate is during 2000–2016. We then show how often, where, and why the super greenhouse effect is produced in section 3.5. Finally, we conclude with a discussion about the results.

2. Data and Methods

2.1. Data

Monthly mean data from CERES EBAF Ed4.1 (Loeb et al., 2018 and Kato et al., 2018), ERA-Interim (Dee et al., 2011), and GFDL AM4 (Zhao et al., 2018) are used to study the temporal variability of ΔG from March 2000 to August 2016. Within Edition 4.1 of CERES EBAF, we use the "t" version: clear sky fluxes from the total area of a region. Uncertainty in CERES EBAF Edition 4's regional monthly clear sky OLR is 4.5–5 W m^{-2} and in the global mean it is approximately 2 W m^{-2} (Loeb et al., 2018). Regional monthly surface upwelling longwave flux (E) uncertainty is 15 W m^{-2} and in the global mean it is 3 W m^{-2} (Kato et al., 2018). In the case of ERA-Interim, surface temperature is used to calculate the surface upwelling flux ($E = \sigma T_s^4$) with the assumption of unit emissivity (Wilber et al., 1999). Outputs from GFDL AM4 are generated using prescribed observed SSTs.

Monthly mean ozone mixing ratio, water vapor mixing ratio, atmospheric temperature, and surface temperature from ERA-I and AM4 are used as inputs for the Rapid Radiative Transfer Model (RRTM; Mlawer et al., 1997) for the partial radiative perturbation (PRP) experiments. The dimensions, units, and resolutions of the relevant quantities are listed in Table 1. For the "ERA+RRTM" PRP experiments, we regrid H_2O, T_a, and T_s onto 2.25° × 2.25° (10° × 10° resolution for "AM4+RRTM") to reduce computational time (Table 1). This yields 2.25° × 2.25° grid box means of G covering the globe.

2.2. Definitions

The time series of ΔG (deseasonalized anomaly) for a particular grid box is found using the following:

Table 1
Description of Quantities Used in Paper

Quantity	Full name	Data set	Dependent variables	Units	Resolution
G^*	Clear Sky Greenhouse Effect	CERES EBAF	(t,x,y)	W m^{-2}	1° × 1°
G^*	Clear Sky Greenhouse Effect	ERA-Interim	(t,x,y)	W m^{-2}	0.75° × 0.75°
G^*	Clear Sky Greenhouse Effect	GFDL AM4	(t,x,y)	W m^{-2}	1.25° × 1°
G^{**}	Clear Sky Greenhouse Effect	ERA+RRTM AM4+RRTM	(t,x,y)	W m^{-2}	2.25° × 2.25° 10° × 10°
T_s^{***}	Surface Temperature	ERA-Interim GFDL AM4	(t,x,y)	K	2.25° × 2.25° 10° × 10°
T_a^{***}	Atmospheric Temperature	ERA-Interim GFDL AM4	(t,x,y,z)	K	2.25° × 2.25° 10° × 10°
H_2O^{***}	Water Vapor Mixing Ratio	ERA-Interim GFDL AM4	(t,x,y,z)	ppmv	2.25° × 2.25° 10° × 10°

Note. Time denoted by "t", longitude denoted by "x", latitude denoted by "y", and height denoted by "z". ERA-Interim has 37 vertical levels and GFDL AM4 has 33 vertical levels. All quantities are monthly means. "*" refers to G derived from existing data set, "**" refers to G calculated using RRTM, and "***" refers to inputs used for radiative transfer calculations in RRTM. "ERA+RRTM" and "AM4+RRTM" spatial resolutions are obtained first by taking area averages at native grid resolution.

$$\Delta G(t,x,y) = G(t,x,y) - G(\bar{t},x,y). \tag{2}$$

Throughout this paper, Δ refers to a temporal anomaly and the overbar denotes a temporal mean at a particular latitude and longitude, unless otherwise stated. For ease of notation, if a quantity (α) is temporally averaged, we shorten $\alpha(\bar{t},x,y,z)$ to $\overline{\alpha}$ and for an anomaly, $\Delta\alpha(t,x,y,z)$ is shortened to $\Delta\alpha$. When several grid boxes of a climatological quantity are averaged to a larger region such as the globe or Tropics, we will explicitly mention $(\overline{x},\overline{y})$ with the quantity.

The Tropics are defined as 30°S to 30°N, the West Pacific as 15°S to 15°N, 90–150°E, and the Central Pacific as 15°S to 5°N, 150–240°E (rectangles in Figure 4a). The West Pacific and Central Pacific are similar in area, and each occupy ~9% of the Tropics. El Niño and La Niña events are classified using the Oceanic Niño Index (ONI), that is, surface temperature anomalies greater than 0.5 K and less than −0.5 K, respectively, for five or more consecutive months in the Niño 3.4 region (5°S to 5°N, 190–240°E) using a 3-month running mean. The troposphere is partitioned into the lower troposphere (surface–700 hPa), middle troposphere (700–400 hPa), and upper troposphere (400–150 hPa).

2.3. Partial Radiative Perturbation Experiments

In order to quantify the drivers of ΔG, we performed nine PRP experiments. The PRP method (e.g., Becker & Stevens, 2014; Colman & McAvaney, 2011; Colman, 2015; Colman et al., 2001; Klocke et al., 2013) assumes that for small perturbations to the climate system, ΔG can be linearly decomposed into its constituents:

$$\Delta G = \Delta G_{H_2O} + \Delta G_{T_a} + \Delta G_{T_s}. \tag{3}$$

The PRP method substitutes each variable from the perturbed climate into the control climate one by one in an off-line radiation code (RRTM). The radiative perturbations, that is, anomalies, on the RHS of equation (3) are then calculated by subtracting off the radiation from the nonperturbed state.

In our study, the control climate refers to the monthly climatology of each variable. Experiment 1 calculates ΔG and experiments 2-4 decompose ΔG into its constituents as shown in equation (4). Similarly, in experiments 5–8, contributions by water vapor (ΔG_{H_2O}) to ΔG are further decomposed into contributions from lower, middle, and upper tropospheric water vapor (equations (5b)–(5d)) and water vapor arising from fixed and varying RH (equations (6c)–(6d)). Lastly, experiment 9 computes the contributions from varying carbon dioxide, methane, and nitrous oxide (section 3.1 and Figure 1).

$$\Delta G = G(H_2O, T_a, T_s) - G(\overline{H_2O}, \overline{T_a}, \overline{T_s}) \tag{4a}$$

$$\Delta G_{H_2O} = G(H_2O, T_a, T_s) - G(\overline{H_2O}, T_a, T_s) \tag{4b}$$

$$\Delta G_{T_a} = G(\overline{H_2O}, T_a, T_s) - G(\overline{H_2O}, \overline{T_a}, T_s) \tag{4c}$$

$$\Delta G_{T_s} = G(\overline{H_2O}, \overline{T_a}, T_s) - G(\overline{H_2O}, \overline{T_a}, \overline{T_s}) \tag{4d}$$

Table 2
Global Mean and Time Mean G Comparison Between Observational, Reanalysis, and Modeling Data Sets Over March 2000 to August 2016

Quantity	ERBE	CE 4.1 "*c*"	CE 4.1 "*t*"	ERA-Interim	GFDL AM4
G_{Oceans}	146 ± 7	131.3 ± 0.5	134.1 ± 0.5	134.8 ± 0.6	135.0 ± 0.5
G	–	129.7 ± 0.6	132.4 ± 0.6	133.1 ± 0.7	133.4 ± 0.6

Note. ERBE's time period was over April 1985 to January 1986. CE 4.1 "*c*" and CE 4.1 "*t*" denote CERES EBAF Edition 4.1 observations using cloud-free areas of a region and the total area of a region, respectively. Units of *G* are in W m^{-2}. Uncertainties in *G* are the 95% confidence intervals.

2.4. Testing the Sensitivity of Experiments

Conducting the PRP experiments in different orders did not make a quantitative difference in our results. We tested the influence of spatial resolution on the results by comparing finer spatial resolution (2.25° × 2.25°) to coarser spatial resolution (10° × 10°) in the ERA+RRTM PRP experiments. We found that the coarser resolution ΔG explained over 99% of the variance in the finer resolution ΔG time series. We tested the sensitivity of our results to radiative computational accuracy by using a line-by-line (LBL) radiative transfer model (Dudhia, 2017) as opposed to a band model (RRTM) for a 10° × 10° grid box in the Central Pacific. Near-perfect agreement ($r^2 = 0.98$) between the LBL calculated and the RRTM calculated ΔG time series was found. The agreement between LBL models and band models has been found in past literature too (Briegleb, 1992). Lastly, we show in Figure S1 in the supporting information that the use of monthly mean profiles with RRTM (AM4+RRTM) is accurate ($r^2 = 0.99$) relative to radiative fluxes calculated from instantaneous profiles and then averaged up to monthly fluxes (AM4 output).

3. Results

3.1. *G* and ΔG in CERES Era

In Table 2, we compare the globally averaged and time-averaged values of *G*, that is, $G(\bar{t}, \bar{x}, \bar{y})$ between data sets. We find that the reanalysis data set, ERA-Interim, and the general circulation model, GFDL AM4, agree to within 1 W m^{-2} of CERES EBAF 4.1 version "*t*" values. Values from CERES EBAF 4.1 version "*c*" are lower than version "*t*" because version "*c*" outputs clear sky fluxes from cloud free areas of a region, which are generally less moist than the grid point's cloudy columns. Version "*t*" contains an adjustment that ignores clouds in the atmospheric column, which makes version "*t*" more consistent with how general circulation models calculate clear sky fluxes (Potter et al., 1992 and Loeb et al., 2018). Values of global mean *G* obtained and derived from other studies such as 135.4 W m^{-2} and 131 W m^{-2} from Huang (2013) and Wild et al. (2018), respectively, are also consistent with Table 2's values.

Note that, over oceans, $G(\bar{t}, \bar{x}, \bar{y})$ from ERBE (Raval & Ramanathan, 1989) is higher than the *G* from each of the modern data sets. This discrepancy is most likely due to the fact that ERBE was not energy balanced like CERES EBAF. Radley et al. (2014) also summarized differences between ERBE and CERES by noting that the satellites had different orbits, data processing techniques, and calibrations, which yielded different OLR values. Detailed explanations regarding the differences between ERBE and the modern data sets is outside the scope of this paper (see Wielicki et al., 2002; Raschke et al., 2012).

Figure 1a shows the seasonal cycle of *G*. The variability of *G* from CERES EBAF (red) is captured by ERA+RRTM (black) and ERA+RRTM_gg (green). In the ERA+RRTM_gg case, varying monthly concentrations of CO_2, CH_4, and N_2O are used. However, in the ERA+RRTM case (black), CO_2, CH_4, and N_2O monthly values are held fixed at 2015's values. The peak of *G* is during Northern Hemispheric (NH) summer and its trough is during NH winter. This is consistent with the NH summer (winter) being hotter (colder) than the Southern Hemisphere's summer (winter), and the fact that *G* is driven by the surface temperature and its accompanying changes in atmospheric temperature and water vapor (section 3.2).

Although *G* has a large seasonal cycle, we are interested in how anomalous *G* is for a given month, so we calculate ΔG using equation (2). In Figure 1b we plot the time series of globally averaged ΔG. This reveals that ΔG's variability from CERES EBAF is reproduced by ERA+RRTM_gg ($r^2 = 0.84$) and ERA+RRTM ($r^2 = 0.77$). The fact that ΔG from ERA+RRTM_gg and ΔG from ERA+RRTM are in agreement ($r^2 = 0.93$) implies that greenhouse gas variations do not impact interannual variability in ΔG. ERA+RRTM_gg is important for explaining trends. The trend in CERES EBAF Ed4.1 "*t*" of 1.07 ± 0.07 W m^{-2}·$decade^{-1}$ is

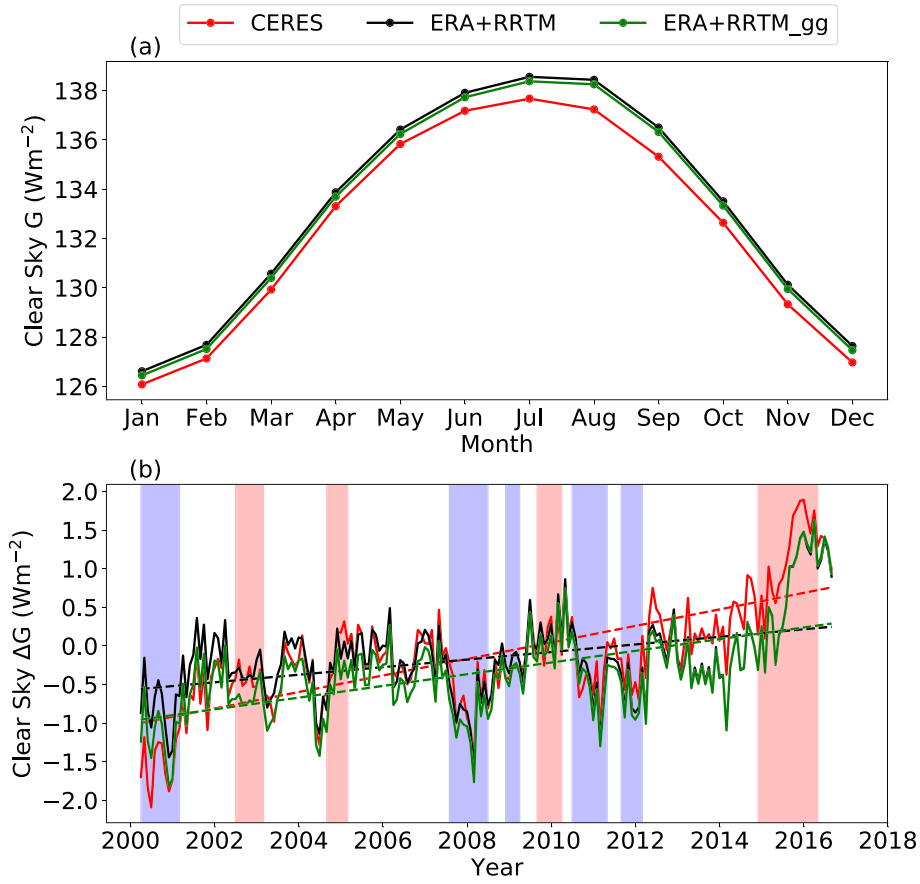

Figure 1. (a) Seasonal cycle of global G over January 2001 to December 2015. (b) Deseasonalized anomalies of global G from March 2000 to August 2016. ERA+RRTM_gg G is calculated from RRTM using ERA-Interim's climatological data with CO_2, CH_4, and N_2O varying (green), ERA+RRTM G is calculated from RRTM using ERA-Interim's climatological data with CO_2, CH_4, and N_2O fixed at 2015's values (black), and satellite observed G is from CERES EBAF Edition 4.1 "t" (red). Light red and blue shadings indicate El Niño and La Niña events, respectively. Dotted lines indicate trends.

better explained by the 0.76 ± 0.07 W m^{-2}·decade^{-1} trend in G with varying greenhouse gas concentration (ERA+RRTM_gg) rather than the 0.49 ± 0.07 W m^{-2}·decade^{-1} trend in G with fixed greenhouse gas concentration (ERA+RRTM). However, since we are interested in the month-to-month and interannual changes, we use ERA+RRTM and not ERA+RRTM_gg for the rest of the paper so as to isolate the effects of changes in surface temperature, atmospheric temperature, and water vapor on ΔG. We repeated the above calculations for ΔG with "AM4+RRTM_gg" and "AM4+RRTM" and found poorer correlations with CERES EBAF ($r^2 = 0.62$ and $r^2 = 0.52$, respectively).

In Figure 1b we observe that the dominant mode of interannual variability in the climate system, the El Niño–Southern Oscillation (ENSO; Trenberth, 1997), shows its imprints on the global ΔG. During a La Niña, such as the 2007–2008 event, Earth becomes colder and consequently G decreases by 1.5 W m^{-2}. Conversely, during an El Niño, such as the 2015–2016 event, Earth becomes warmer and consequently G increases by 1.8 W m^{-2}. In the next section, we discuss how these changes in G arise by decomposing ΔG into its constituents, in particular during ENSO events.

3.2. Breakdown of ΔG

The time series of ΔG is broken down into contributions from surface temperature (purple), atmospheric temperature (gray), and water vapor (orange; Figure 2a) using the ERA+RRTM experiments (equation (4)). ΔG_{T_s} can be interpreted as the "passive" atmosphere contribution—the atmosphere absorbs upwelling photons associated with surface temperature changes while the atmospheric state stays fixed. The maximum ΔG_{T_s} can be $E = \sigma T_s^4$. In turn, ΔG_{T_a} loses photons to space, which acts to balance ΔG_{T_s}. To the first order, this

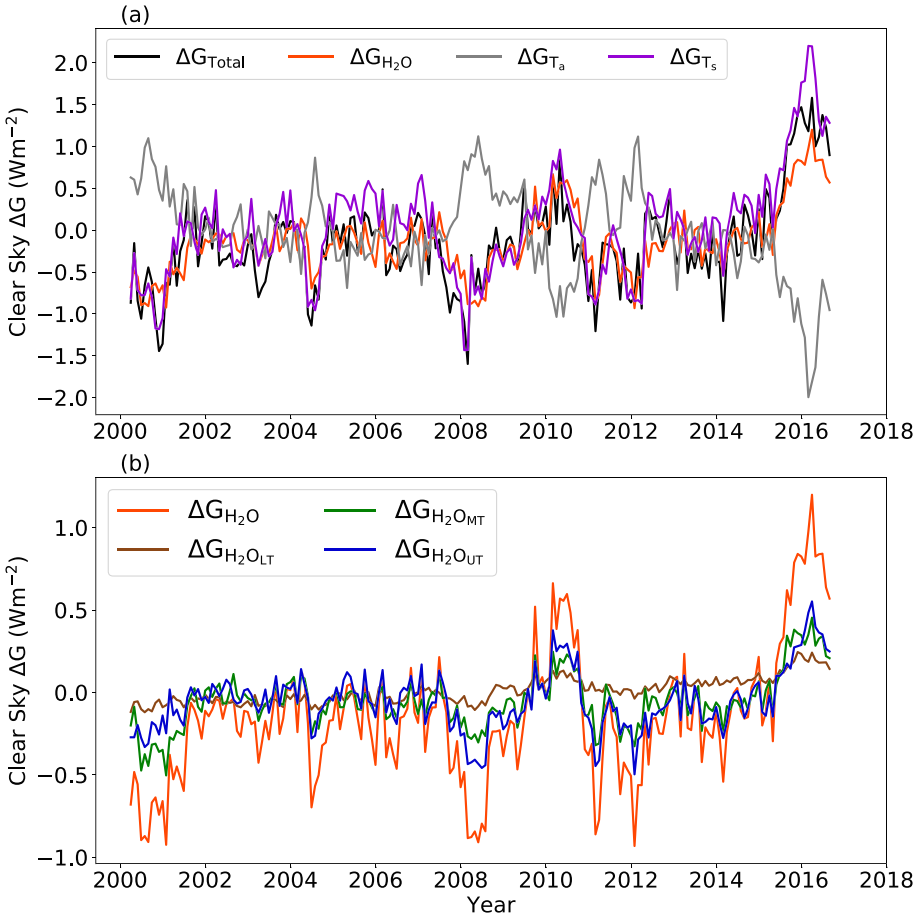

Figure 2. Breakdown of globally averaged ΔG using ERA-Interim climatological data in RRTM. (a) Contributions from water vapor, atmospheric temperature, and surface temperature. (b) Contributions from lower (surface–700 hPa), middle (700–400 hPa), and upper (400–150 hPa) tropospheric water vapor.

balance determines the greenhouse effect—the atmospheric temperature is colder than the surface temperature, leading to radiation being trapped in the atmosphere. In addition, $\Delta G_{\mathrm{H_2O}}$ acts to increase the radiation trapped by the atmosphere.

As seen in Figure 2a, all three components are important in contributing to the overall anomaly in G each month. This is further seen in Table 3, which decomposes ΔG into its components during ENSO events. Here, we took a spatial average of each quantity and then did a temporal average only during ENSO events.

Table 3
Breakdown of $\Delta G(\bar{t}, \bar{x}, \bar{y})$ During a Composite of ENSO Events Using ERA-Interim Climatological Data as Input for RRTM

Region	Time	ΔG_{Total}	$\Delta G_{\mathrm{H_2O}}$	ΔG_{T_a}	ΔG_{T_s}
Global	El Niño	0.21 ± 0.19	0.16 ± 0.13	-0.44 ± 0.17	0.49 ± 0.22
	La Niña	-0.61 ± 0.11	-0.46 ± 0.11	0.41 ± 0.13	-0.56 ± 0.11
Tropical	El Niño	0.51 ± 0.24	0.25 ± 0.20	-0.73 ± 0.28	0.99 ± 0.29
	La Niña	-1.02 ± 0.18	-0.70 ± 0.16	0.73 ± 0.17	-1.04 ± 0.16
West Pacific	El Niño	-2.22 ± 0.60	-2.08 ± 0.55	-0.36 ± 0.30	0.22 ± 0.31
	La Niña	1.38 ± 0.66	1.12 ± 0.52	0.42 ± 0.21	-0.15 ± 0.37
Central Pacific	El Niño	4.21 ± 0.84	2.93 ± 0.81	-1.50 ± 0.37	2.78 ± 0.38
	La Niña	-5.13 ± 0.74	-3.56 ± 0.58	1.69 ± 0.28	-3.25 ± 0.44

Note. Units of ΔG are in W m^{-2}. Uncertainties are 95% confidence intervals.

Table 4
Vertical Breakdown of $\Delta G_{H_2O}(\bar{t}, \bar{x}, \bar{y})$ *During a Composite of ENSO Events Using ERA-Interim Climatological Data as Input for RRTM*

Region	Time	ΔG_{H_2O}	$\Delta G_{H_2O_{LT}}$	$\Delta G_{H_2O_{MT}}$	$\Delta G_{H_2O_{UT}}$
Global	El Niño	0.16 ± 0.13	0.06 ± 0.03	0.07 ± 0.05	0.08 ± 0.05
	La Niña	-0.46 ± 0.11	-0.02 ± 0.02	-0.18 ± 0.05	-0.19 ± 0.05
Tropical	El Niño	0.25 ± 0.20	0.10 ± 0.05	0.12 ± 0.08	0.10 ± 0.08
	La Niña	-0.70 ± 0.16	-0.04 ± 0.03	-0.24 ± 0.07	-0.32 ± 0.07
West Pacific	El Niño	-2.08 ± 0.55	-0.16 ± 0.07	-1.1 ± 0.29	-0.74 ± 0.22
	La Niña	1.12 ± 0.52	0.18 ± 0.09	0.73 ± 0.28	0.32 ± 0.19
Central Pacific	El Niño	2.93 ± 0.81	0.56 ± 0.14	1.56 ± 0.41	0.98 ± 0.32
	La Niña	-3.56 ± 0.58	-0.46 ± 0.07	-1.67 ± 0.28	-1.27 ± 0.23

Note. Lower troposphere (surface–700 hPa) denoted by "LT", middle troposphere (700–400 hPa) denoted by "MT", and upper troposphere (400–150 hPa) denoted by "UT". Units of ΔG are in W m^{-2}. Uncertainties are 95% confidence intervals.

The ΔG_{T_s} and ΔG_{H_2O} components are of the same sign (barring the West Pacific) and are offset partially by the ΔG_{T_a} component of the opposite sign. The magnitude of the offset varies in location and ENSO events. These results are largely consistent with "AM4+RRTM" (supporting information's Figure S2 and Table S1).

We have quantitatively shown that the radiative contribution by water vapor is important for explaining the greenhouse effect anomaly (Figure 2a and Table 3). To understand the reasons for water vapor's radiative contributions, we break down ΔG_{H_2O} into contributions from water vapor in the lower troposphere (LT), middle troposphere (MT), and upper troposphere (UT) using the PRP method (equation (5) and section 2.3).

$$\Delta G_{H_2O} = G(H_2O, T_a, T_s) - G(\overline{H_2O}, T_a, T_s) \tag{5a}$$

$$\Delta G_{H_2O_{LT}} = G(H_2O_{LT}, \overline{H_2O_{MT}}, \overline{H_2O_{UT}}, T_a, T_s) - G(\overline{H_2O}, T_a, T_s) \tag{5b}$$

$$\Delta G_{H_2O_{MT}} = G(\overline{H_2O_{LT}}, H_2O_{MT}, \overline{H_2O_{UT}}, T_a, T_s) - G(\overline{H_2O}, T_a, T_s) \tag{5c}$$

$$\Delta G_{H_2O_{UT}} = G(\overline{H_2O_{LT}}, \overline{H_2O_{MT}}, H_2O_{UT}, T_a, T_s) - G(\overline{H_2O}, T_a, T_s) \tag{5d}$$

In Figure 2b we plot the time series of vertical partitioning of global ΔG_{H_2O}. Results indicate that throughout the time series, the middle troposphere (green) and upper troposphere (dark blue) contribute nearly equally to global ΔG_{H_2O}. Earlier in the time series, MT contributes more than UT to ΔG_{H_2O}. During ENSO events, MT again contributes more than UT, but only leading up to the peak. At the peak, UT contributes more than MT to ΔG_{H_2O}. In comparison, "AM4+RRTM" (Figure S2) shows that MT and UT contribute equally to ΔG_{H_2O} throughout the duration of ENSO events. The vertical breakdown of water vapor's contributions to ΔG during ENSO events is further quantified in Table 4. This breakdown demonstrates that the middle troposphere and upper troposphere contribute equally to ΔG_{H_2O} not just in localized regions such as the West Pacific or Central Pacific but in the global mean and tropical mean as well. During El Niño events, lower tropospheric contributions are also comparable to the middle and upper tropospheric contributions in the globe-wide and tropics-wide cases. For both El Niño and La Niña events, middle tropospheric water vapor contributions far exceed lower and upper tropospheric water vapor contributions in the West Pacific and Central Pacific.

3.3. How Accurate Is the Fixed Relative Humidity Assumption for ΔG?

This section investigates the impact of fixed and varying relative humidity (RH) on ΔG_{H_2O}. We breakdown ΔG_{H_2O} into $\Delta G_{H_2O_{FRH}}$ and $\Delta G_{H_2O_{VRH}}$ for each $2.25° \times 2.25°$ grid box.

$$e_{sat}(T) = 611 \times \exp\left(\frac{17.625T}{T + 243.04}\right) \text{Pa} \tag{6a}$$

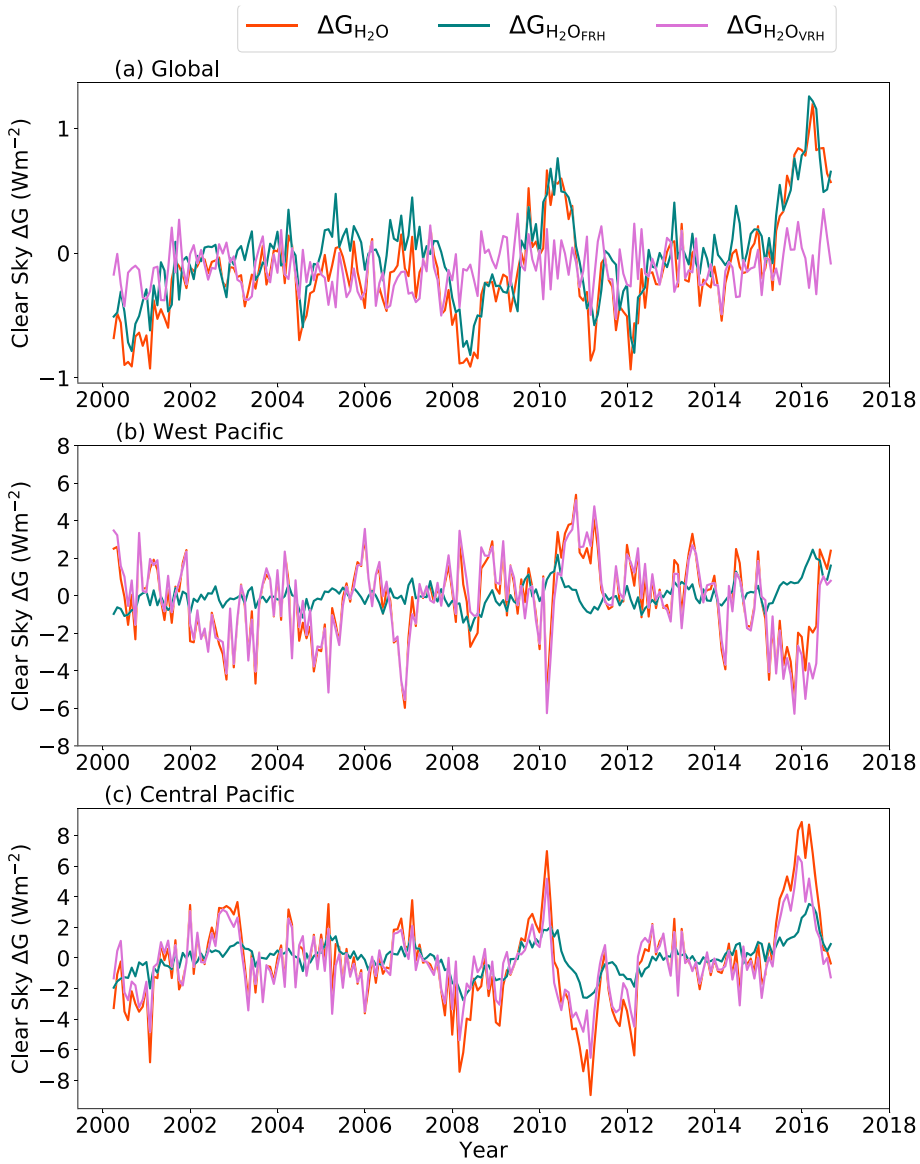

Figure 3. Contributions to ΔG_{H_2O} by water vapor with fixed and varying RH. (a) Global. (b) West Pacific. (c) Central Pacific.

$$H_2O^* = e_{sat}(T) \times \frac{\overline{H_2O}}{e_{sat}(\overline{T})} \tag{6b}$$

$$\Delta G_{H_2O_{FRH}} = G(H_2O^*, T_a, T_s) - G(\overline{H_2O}, T_a, T_s) \tag{6c}$$

$$\Delta G_{H_2O_{VRH}} = G(H_2O, T_a, T_s) - G|(H_2O^*, T_a, T_s) \tag{6d}$$

We obtain the saturation vapor pressure from the Claussius-Clapeyron equation (equation (6a)). To obtain the "fixed RH," that is, the monthly climatology RH, we find the ratio of the monthly climatology of water vapor ($\overline{H_2O}$) and the monthly climatology of the saturation vapor pressure ($e_{sat}(\overline{T})$). Equation (6b) yields water vapor that is driven by varying T while holding RH fixed (H_2O^*). We then use these as inputs for RRTM for our PRP experiments (section 2.3) to obtain $\Delta G_{H_2O_{FRH}}$ and $\Delta G_{H_2O_{VRH}}$ (equations (6c) and (6d)).

Figure 3a displays the globally averaged ΔG_{H_2O} (orange) and its contributions from $\Delta G_{H_2O_{FRH}}$ (teal) and $\Delta G_{H_2O_{VRH}}$ (light pink). The variability of ΔG_{H_2O} can be captured by ERA+RRTM when RH is fixed, which

Table 5
Spatially Averaged Contributions to ΔG_{H_2O} by Water Vapor with Fixed and Varying RH During a Composite of ENSO Events Using ERA-Interim Climatological Data as Input for RRTM

Region	Time	ΔG_{H_2O}	$\Delta G_{H_2O_{FRH}}$	$\Delta G_{H_2O_{VRH}}$
Global	El Niño	0.16 ± 0.13	0.25 ± 0.12	-0.09 ± 0.05
	La Niña	-0.46 ± 0.11	-0.31 ± 0.09	-0.15 ± 0.05
Tropical	El Niño	0.25 ± 0.20	0.52 ± 0.20	-0.28 ± 0.09
	La Niña	-0.70 ± 0.16	-0.55 ± 0.13	-0.16 ± 0.09
West Pacific	El Niño	-2.08 ± 0.55	0.32 ± 0.23	-2.39 ± 0.58
	La Niña	1.12 ± 0.52	-0.37 ± 0.16	1.49 ± 0.46
Central Pacific	El Niño	2.93 ± 0.81	1.10 ± 0.27	1.84 ± 0.62
	La Niña	-3.56 ± 0.58	-1.23 ± 0.22	-2.33 ± 0.48

Note. Units of ΔG are in W m^{-2}.

is evidenced by the overlap between ΔG_{H_2O} and $\Delta G_{H_2O_{FRH}}$ ($r^2 = 0.8$). This implies that knowing the changes in surface and atmospheric temperatures in each grid box is sufficient to calculate global ΔG_{H_2O}, without needing to account for varying RH associated with dynamic changes. This implies that global ΔG can also be found from surface and atmospheric temperatures alone. Figure 3a shows that the fixed RH approximation is especially accurate during ENSO events (La Niñas in 2000–2001 and 2007–2008; El Niños in 2009–2010 and 2015–2016). During El Niño, the global ΔG_{H_2O} is dominated by the fixed RH contributions (Table 5).

Although assuming fixed RH for each grid box yielded a globally averaged $\Delta G_{H_2O_{FRH}} \approx \Delta G_{H_2O}$, smaller regions are known to exhibit large shifts in RH (Dessler et al., 2008). For smaller regions, the variability in radiative contributions by water vapor can be explained by the contributions from water vapor arising from varying RH and not by fixed RH. For example, in Figure 3b's West Pacific case, $\Delta G_{H_2O_{VRH}}$ explains 92% of ΔG_{H_2O}'s variance ($r^2 = 0.92$). In the last two rows of Table 5 we further see that varying RH plays a much bigger role locally, with 60–70% of ΔG_{H_2O} coming from $\Delta G_{H_2O_{VRH}}$. Spatial maps of ΔG (Figures 4a and 4b), $\Delta G_{H_2O_{VRH}}$ (Figures 4c and 4d), and $\Delta G_{H_2O_{FRH}}$ (Figures 4d and 4e) demonstrate this result further. Readers interested in the spatial patterns of ΔG's breakdown into ΔG_{H_2O}, ΔG_{T_a}, and ΔG_{T_s} can view Figure S5 in the supporting information.

During ENSO events, the spatial pattern of $\Delta G_{H_2O_{VRH}}$ matches that of ΔG, because, locally, varying RH contributions dominate ΔG_{H_2O}, which in turn is a significant contributor to ΔG. The spatial pattern of $\Delta G_{H_2O_{FRH}}$ does not resemble that of $\Delta G_{H_2O_{VRH}}$ and ΔG (the latter two quantities match the canonical ENSO SST pattern ; Trenberth, 1997), signaling that, locally, $\Delta G_{H_2O_{FRH}}$ is a poor assumption at each grid box. This implies that changes in the temperature will not be a good indicator of how G will change. To accurately know how G will change locally, information on variations in RH are needed. Results from AM4+RRTM in supporting information Figures S3 and S4 and Table S2 agree with these findings.

Local cancelations in $\Delta G_{H_2O_{VRH}}$ result in a near-zero global mean $\Delta G_{H_2O_{VRH}}$. This can also be seen in Figures 3b and 3c in which the West Pacific and Central Pacific's varying RH contributions largely cancel each other out. For example, during El Niño 2015–2016, $\Delta G_{H_2O_{VRH}}$ is approximately -6 W m^{-2} in the West Pacific and $+5$ W m^{-2} in Central Pacific. These cancelations render the global $\Delta G_{H_2O_{VRH}}$ insignificant, leaving $\Delta G_{H_2O_{FRH}}$ as the major contributor to ΔG_{H_2O}. In the next section, we will see that the fixed RH approximation for global ΔG_{H_2O} extends to its sensitivity to surface temperature. In section 3.5 we will demonstrate that the radiative contributions from varying RH are crucial for generating the super greenhouse effect.

3.4. Sensitivity of G and ΔG to Surface Temperature

In this section, we apply two methods to determine the sensitivity of G and ΔG to surface temperature (T_s) and also breakdown $\Delta G'$ s sensitivity to ΔT_s into its components. Raval and Ramanathan (1989) calculated the sensitivity of all sky G to surface temperature by obtaining the slope from a linear least squares regression between G (4-month mean from 1985–1986) and SST over all spatial points. We replicate this method and regress clear sky G and T_s across all latitudes and longitudes (land and ocean) to obtain $\frac{dG(\bar{t},x,y)}{dT_s(\bar{t},x,y)}$ (Figure 5a). We take the mean of all months of clear sky G and T_s from March 2000 to August 2016, using CERES EBAF data. Surface temperature is approximated by taking the inverse of the Stefan-Boltzmann law ($T_s = (\frac{E}{\sigma})^{1/4}$)

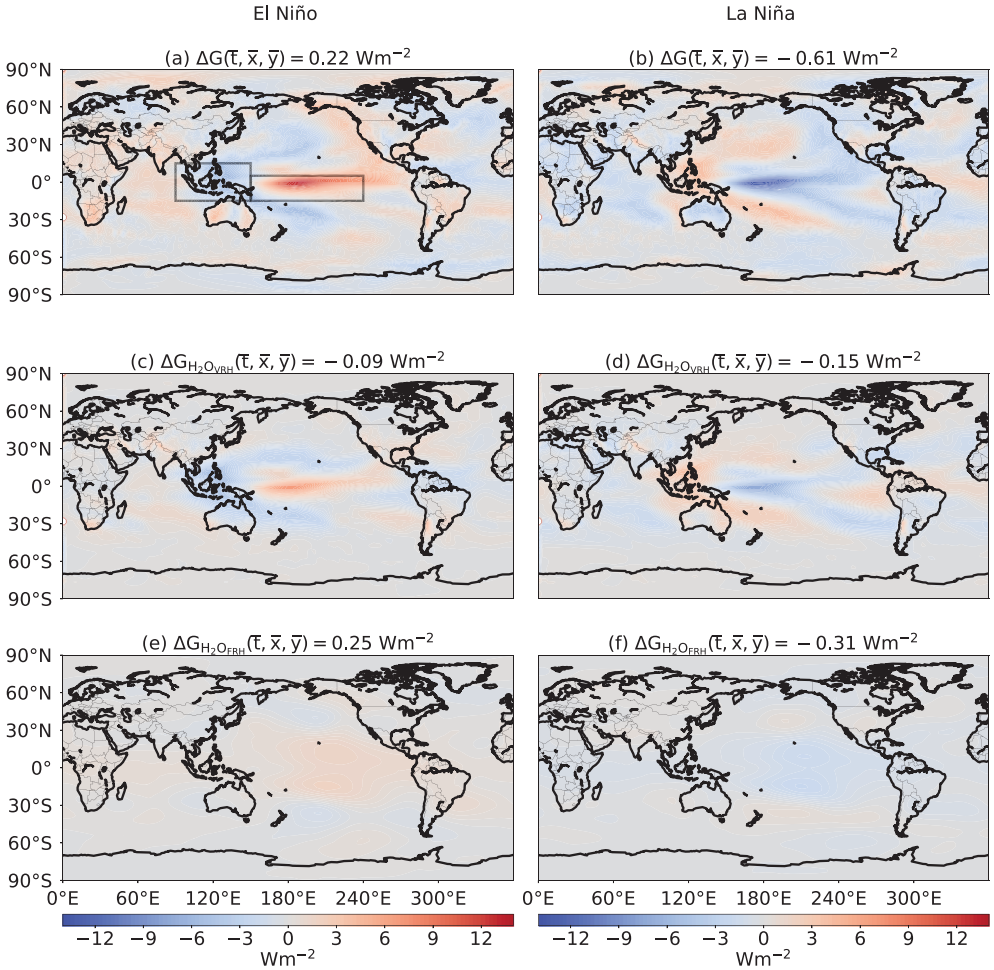

Figure 4. Spatial anomalies in the clear sky greenhouse effect during a composite of El Niño and La Niña events from March 2000 to August 2016 using ERA-Interim climatological data as input for RRTM. El Niño events on the left column and La Niña events on the right column. (a, b) ΔG. (c, d) Contributions to ΔG_{H_2O} by water vapor arising from varying RH alone. (e, f) Contributions to ΔG_{H_2O} by water vapor arising from fixed RH alone. Sum of (c) and (e) (similarly for (d) and (f)) yields ΔG_{H_2O}, that is, water vapor's contribution to ΔG.

for this data set. We apply this method to multiple data sets in Table 6, which yields similar values in the range of 2.4–2.5 W m^{-2} K^{-1}. The surface temperatures used for regression in ERA-I, ERA+RRTM, AM4, and AM4+RRTM are directly from skin temperatures in the ERA-I and AM4 data sets, respectively.

We find that G is a nonlinear function of T_s and hence using a linear fit does not capture the extremes of the curve (Figure 5a). The method by Raval and Ramanathan (1989) correlates unrelated spatial regions, which masks important differences in underlying physics. For example, parts of the West Pacific warm pool and the Sahara Desert have similar surface temperatures ($\approx$ 300 K), but they have wildly different values for G due to different humidity conditions ($\approx$ 210 W m^{-2} over West Pacific and $\approx$ 150 W m^{-2} over Sahara Desert). Thus, the slope obtained from regressing across such different regions together misrepresents the sensitivity of G to T_s for Earth.

To be consistent with how radiative sensitivities to surface temperature are calculated (Andrews et al., 2012; Otto et al., 2013), we regress the time series of the globally averaged $\Delta G(t, \bar{x}, \bar{y})$ against $\Delta T_s(t, \bar{x}, \bar{y})$ to obtain $\frac{d\Delta G(t,\bar{x},\bar{y})}{d\Delta T_s(t,\bar{x},\bar{y})}$ (Figure 5b). This method weights different spatial points appropriately and yields a representative "global column." This method yields an observed sensitivity of 3.96 W m^{-2} K^{-1} when using CERES EBAF 4.1 "t" data. This sensitivity is 0.42 W m^{-2} K^{-1} higher than the sensitivity of CERES EBAF 4.1 "c," demonstrating that the method used to obtain clear sky fluxes, either from ignoring clouds in the atmospheric column or sampling cloud free regions, impacts the sensitivity of global mean G to global mean surface temperature.

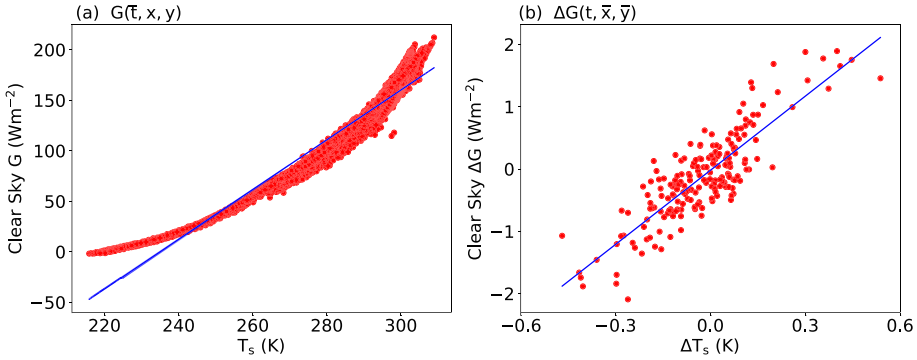

Figure 5. Sensitivity of G and ΔG to surface temperature using CERES EBAF 4.1 "t" from March 2000 to August 2016. (a) Spatial regression: $G(\bar{t}, x, y)$ regressed against $T_s(\bar{t}, x, y)$. Sensitivity given by slope of the linear regression, that is, $\frac{dG(\bar{t},x,y)}{dT_s(\bar{t},x,y)} = 2.46$ W m^{-2} K^{-1}. (b) Temporal regression: $\Delta G(t, \bar{x}, \bar{y})$ regressed against $\Delta T_s(t, \bar{x}, \bar{y})$. Sensitivity given by slope of the linear regression, that is, $\frac{d\Delta G(t,\bar{x},\bar{y})}{d\Delta T_s(t,\bar{x},\bar{y})} = 3.96$ W m^{-2} K^{-1}.

The standard error associated with these gradients increases as the number of data points decreases (O(10^4) for $\frac{dG(\bar{t},x,y)}{dT_s(\bar{t},x,y)}$ and O(10^2) for $\frac{d\Delta G(t,\bar{x},\bar{y})}{d\Delta T_s(t,\bar{x},\bar{y})}$).

When variations in greenhouse gases are included, the ERA+RRTM sensitivity (Table 6) increases from 3.13 to 3.47 W m^{-2} K^{-1}. Similarly, the AM4+RRTM sensitivity increases from 3.10 to 3.33 W m^{-2} K^{-1} and the sensitivity from AM4's output increases from 3.17 to 3.40 W m^{-2} K^{-1}. The sensitivities with greenhouse gas variations included (3.33–3.47 W m^{-2} K^{-1}), are closer to CERES EBAF's estimates, implying that the greenhouse gas forcing from 2000 to 2016 is important in explaining the observed sensitivity of the global clear sky greenhouse effect to surface temperature. As mentioned earlier, CERES EBAF 4.1 version "t" is consistent with how general circulation models compute clear sky fluxes, so it is intriguing that the estimate of sensitivity from version "t" is further from models and reanalysis estimates as compared to the estimate from version "c". ERA-I's output produces an abnormally low sensitivity of 1.1 W m^{-2} K^{-1}. This discrepancy arises due to abruptly occurring large anomalies in ERA-I's time series of ΔG (Figure S6). This results in a larger spread and thus a lower sensitivity.

An application of the linear sensitivities obtained in Table 6 is that we can estimate ΔG using the sensitivity and surface temperature change. The monthly values of ΔG calculated using the linear sensitivity and surface temperature change captures the variability of ΔG obtained by full radiative transfer calculations ($r^2 = 0.8$). For example, for an increase of 0.5 K in surface temperature during El Niño 2015–2016, we expect the anomalous total greenhouse trapping to rise by 3.13 W m^{-2} K^{-1} × 0.5 K = 1.57 W m^{-2}. This increase is precisely recorded in early 2016 for ΔG (Figure 1b).

Next, we decompose $\frac{d\Delta G(t,\bar{x},\bar{y})}{d\Delta T_s(t,\bar{x},\bar{y})}$ into its contributions from water vapor, atmospheric temperature, and surface temperature with ERA+RRTM. To obtain these sensitivities, we regress ΔG's monthly means for each

Table 6
Comparison of Gs and OLRs Sensitivity to Surface Temperature Between Observational, Reanalysis, and Modeling Data Sets From March 2000 to August 2016

Quantity	CE 4.1 "c"	CE 4.1 "t"	ERA-I	AM4	ERA+RRTM	AM4+RRTM
$\frac{dG(t,x,y)}{dT_s(\bar{t},x,y)}$	2.38 ± 0.002	2.46 ± 0.002	2.50 ± 0.002	2.45 ± 0.002	2.58 ± 0.02	2.54 ± 0.02
$\frac{d\Delta G(t,\bar{x},\bar{y})}{d\Delta T_s(t,\bar{x},\bar{y})}$	3.54 ± 0.15	3.96 ± 0.17	1.13 ± 0.79	3.17 ± 0.12	3.13 ± 0.13	3.10 ± 0.11
$\frac{d\Delta OLR(t,\bar{x},\bar{y})}{d\Delta T_s(t,\bar{x},\bar{y})}$	1.50 ± 0.14	1.15 ± 0.16	4.02 ± 0.81	1.93 ± 0.10	2.02 ± 0.11	1.95 ± 0.10

Note. CE 4.1 "c" and CE 4.1 "t" denote CERES EBAF Edition 4.1 observations using cloud-free areas of a region and the total area of a region, respectively. Units are in W m^{-2} K^{-1}. Uncertainties are given by standard errors. Note that CERES EBAF and ERA-I include changes in G or OLR due to varying greenhouse gas concentrations.

component against ΔT_s's monthly means.

$$\frac{d\Delta G_{Total}}{d\Delta T_s} = \frac{\partial \Delta G_{H_2O}}{\partial \Delta T_s} + \frac{\partial \Delta G_{T_a}}{\partial \Delta T_s} + \frac{\partial \Delta G_{T_s}}{\partial \Delta T_s} \tag{7a}$$

$$3.13 \quad W\,m^{-2}K^{-1} = 1.95 \quad W\,m^{-2}K^{-1} - 2.70 \quad W\,m^{-2}K^{-1} + 3.88 \quad W\,m^{-2}K^{-1} \tag{7b}$$

The standard errors for each term in equation (7b) is approximately 0.1 W m^{-2} K^{-1}. A positive slope of $\frac{\partial \Delta G_{T_s}}{\partial \Delta T_s}$ is expected since if T_s increases then $E = \sigma T_s^4$ increases, which increases G. In contrast, a negative slope of $\frac{\partial \Delta G_{T_a}}{\partial \Delta T_s}$ is expected since if T_a increases then OLR increases. Lastly, a positive slope of $\frac{\partial \Delta G_{H_2O}}{\partial \Delta T_s}$ is expected since if H_2O increases then OLR decreases. The results from section 3.3, $\Delta G_{H_2O} \approx \Delta G_{H_2O_{FRH}}$ (globally), applies to sensitivity to surface temperature as well. We find that $\frac{\partial \Delta G_{H_2O_{FRH}}}{\partial \Delta T_s} = 1.81 \quad W\,m^{-2}K^{-1}$ is nearly equal to $\frac{\partial \Delta G_{H_2O}}{\partial \Delta T_s} = 1.95 \quad W\,m^{-2}K^{-1}$ (equation (7b)).

The method used to obtain $\frac{d\Delta G(t,\bar{x},\bar{y})}{d\Delta T_s(t,\bar{x},\bar{y})}$ (Figure 5b) can also be used to obtain the sensitivity of global mean OLR to surface temperature changes, $\frac{d\Delta OLR(t,\bar{x},\bar{y})}{d\Delta T_s(t,\bar{x},\bar{y})}$ (Table 6). A positive sensitivity for OLR implies that the system loses energy with warming according to the sign notation used in our paper, where upward radiation denotes positive values. The CERES EBAF sensitivities include the radiative forcing due to changes in greenhouse gases and the response of the Earth system to these changes from 2000 to 2016. We estimate the radiative forcing by differencing $\frac{d\Delta OLR(t,\bar{x},\bar{y})}{d\Delta T_s(t,\bar{x},\bar{y})}$ from ERA+RRTM and ERA+RRTM_gg. This suggests that the trend in greenhouse gas forcing from 2000 to 2016 can yield a 0.34 W m^{-2} K^{-1} radiative forcing sensitivity. Applying this correction to the two values from CERES EBAF 4.1 versions "*c*" and "*t*" gives an estimate of the clear sky longwave (LW) feedback of 1.84 and 1.49 W m^{-2} K^{-1}, respectively. The $\frac{d\Delta OLR(t,\bar{x},\bar{y})}{d\Delta T_s(t,\bar{x},\bar{y})}$ sensitivities of AM4, ERA+RRTM, and AM4+RRTM are estimates of the clear sky LW feedback since forcing is fixed (Table 6). Thus, the range of estimates of the clear sky LW feedback parameter we obtain is 1.49–2.02 W m^{-2} K^{-1}. Much of this spread arises from CERES EBAF's cloud clearing mechanism in Edition 4.1 version "*t*," suggesting that it is difficult to constrain the clear sky LW feedback. The observed value from CERES EBAF Ed 4.1 "*t*" is much more sensitive than the reanalysis and model estimates. The clear sky LW feedback inferred from Dessler (2013), which used observations over 2000–2013, is 1.91 W m^{-2} K^{-1}. This estimate lies at the "less" (more OLR escaping with our sign convention) sensitive end of our range.

The ERA+RRTM sensitivity is broken down into contributions from water vapor ($\frac{\partial \Delta OLR_{H_2O}}{\partial \Delta T_s} = -1.95 \quad W\,m^{-2}K^{-1}$, negative of equation (7b)'s respective term), atmospheric temperature ($\frac{\partial \Delta OLR_{T_a}}{\partial \Delta T_s} = 2.70 \quad W\,m^{-2}K^{-1}$, negative of equation (7b)'s respective term), and surface temperature ($\frac{\partial \Delta OLR_{T_s}}{\partial \Delta T_s} = 1.27 \quad W\,m^{-2}K^{-1}$). Koll and Cronin (2018) used an idealized atmospheric column and showed that there was a near-perfect cancelation between the contributions from water vapor and atmospheric temperature to the feedback parameter, and only surface temperature contributes. However, in our ERA+RRTM calculations with real atmospheric conditions for columns across Earth, we show that this cancelation is imperfect with a 37% ($\frac{2.70-1.95}{2.02}$) contribution from atmospheric temperature to the total feedback parameter. This implies that while changes in surface temperature are still the dominant contributor to changes in OLR ($\frac{1.27}{2.02} = 63\%$) as posited by Koll and Cronin (2018), atmospheric temperature plays an important role by outweighing water vapor's contributions. In the next section, we will see that locally, water vapor's radiative contributions overwhelm atmospheric temperature's contributions, which in turn helps generate the super greenhouse effect.

3.5. Super Greenhouse Effect

As mentioned in section 1, the clear sky SGE is defined as an event in which the rate of increase of G with surface temperature (T_s) exceeds the surface emission's rate or, equivalently, when OLR and T_s are anticorrelated (Hallberg & Inamdar, 1993; Stephens et al., 2016; Valero et al., 1997).

$$\frac{dG}{dT_s} - \frac{dE}{dT_s} > 0 \quad \equiv \frac{dOLR}{dT_s} < 0 \tag{7b}$$

Here, we apply a definition of anomalous SGE, that does not depend on SST thresholds or gradients of SST, to investigate how often it occurs, how much of Earth's area experiences it, and how much the areas that

Table 7
Percentage of Area (Region) Exhibiting the Super Greenhouse Effect and Its Contribution to $|\Delta G|$ Using CERES EBAF 4.1 "t" Data from March 2000 to August 2016

Region	$A_{SGE}(\%)$	$\lvert\Delta G_{SGE}\rvert$	$\lvert\Delta G_{non\text{-}SGE}\rvert$	$\lvert\Delta G\rvert$
Global	36	0.38	0.16	0.54
Tropics	46	0.62	0.15	0.77
West Pacific	49	1.59	0.35	1.94
Central Pacific	56	2.81	0.37	3.18

Note. Units of $\Delta G(\bar{t}, \bar{x}, \bar{y})$ are in W m^{-2}.

exhibit SGE contribute to ΔG. We do not define SGE as a rate, but instead define SGE in terms of anomalies, that is, when ΔOLR and ΔT_s are of opposite signs to each other for a particular month and location.

$$\frac{\Delta \mathrm{OLR}(t,x,y)}{\Delta T_s(t,x,y)} < 0 \tag{7b}$$

Thus, when SGE occurs with $\Delta T_s > 0$ and ΔOLR < 0, excess infrared radiation is trapped in the column and the atmosphere loses its ability to cool efficiently. On the other hand, when SGE occurs with $\Delta T_s < 0$ and ΔOLR > 0, the atmosphere cools more efficiently.

We investigate the percentage of Earth's area that is observed to experience SGE from March 2000 to August 2016 using observations from CERES EBAF 4.1 "t" data. For each month we calculate how many grid points satisfy equation (7b) and obtain the percentage of Earth's area that exhibits SGE. Next, we calculate the average percentage of area over the time series, tabulated under A_{SGE} in Table 7. We find that on average for any month during this time period, 36% of Earth's area experiences SGE. We also calculate the percentage of area exhibiting SGE, while restricting our domains to Tropics, West Pacific, and Central Pacific (Table 7). We find that nearly half (46%) of the tropics is in a SGE state.

Since much of Earth's area is experiencing SGE, we plot the frequency of occurrence of SGE at each grid point in Figure 6 to understand the spatial distribution of SGE. Results reveal that there is a high occurrence (up to 80% of the time period) of SGE in the tropics (Figure 6). We observe that there is a clear land-sea contrast, which is consistent with less water vapor over land. The lower occurrence off the coast of South America is likely because of colder SSTs in upwelling regions and less convection, in comparison to the Indo-Pacific region and the Central Pacific. Since our definition of SGE (equation (7b)) uses deseasonalized anomalies, an ENSO pattern is observed in the Central Pacific. When we use nondeseasonalized anomalies in equation (7b), we observe the spatial pattern of the seasonal cycle of SGE (not shown). High frequency of occurrence is observed over the Northern and Southern Hemisphere ITCZ bands, the Bay of Bengal, and the Amazon rainforest. These areas coincide with seasonal high humidity conditions.

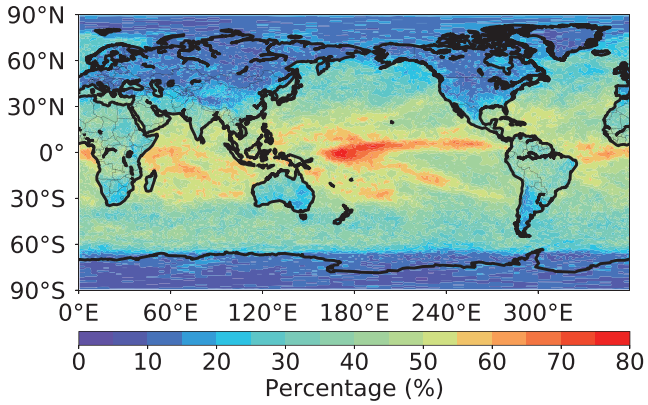

Figure 6. Frequency of super greenhouse effect at each latitude and longitude ($f_{SGE}(x,y)$) using CERES EBAF 4.1 "t" data from March 2000 to August 2016.

Table 8
Percentage of Area (Region) Exhibiting the Super Greenhouse Effect With Water Vapor Arising From Fixed RH Alone (Column 2) and Varying RH Included (Column 3) From March 2000 to August 2016 Using ERA-I Climatological Data as Input for RRTM

Region	$A_{SGE\,\mathrm{FRH}}$	A_{SGE}
Global	15	34
Tropics	15	44
West Pacific	19	46
Central Pacific	13	56

Note. Units of A are in %.

To understand the importance of SGE, we quantify how much SGE contributes to the total magnitude of ΔG, that is, $|\Delta G|$. For each month, we calculate $|\Delta G|$ arising from areas that exhibit SGE (Table 7). By design, taking the temporal mean of ΔG would yield zero, so we take the mean of $|\Delta G|$ to obtain a value that represents the full time series' variability. We find that for the entire time period, the globally averaged $|\Delta G_{\mathrm{SGE}}|$ is 0.38 W m^{-2} and $|\Delta G|$ is 0.54 W m^{-2}. This implies that just over a third of Earth's area (36%) contributes to over two-thirds ($\frac{0.38}{0.54} \approx 70\%$) of the global $|\Delta G|$. Thus, these SGE regions are nearly twice as powerful the non-SGE regions in contributing to greenhouse trapping. Over small regions such as the Central Pacific, 56% of the region exhibits SGE and contributes to 88% of $|\Delta G|$, that is, half the area is contributing to nearly all of the average $|\Delta G|$.

To explain why SGE occurs, we take a twofold approach in demonstrating the importance of water vapor in generating the SGE: (1) by showing how variations in RH impact A_{SGE} and (2) how water vapor at various altitudes differentially impact the total radiative contributions. We use the ERA+RRTM methods from section 3.3 to obtain the dependence of SGE on RH changes. We calculate the total anomalous OLR with fixed RH, that is, $\Delta\mathrm{OLR}_{\mathrm{FRH}} = \mathrm{OLR}(\mathrm{H_2O}^*, T_a, T_s) - \mathrm{OLR}(\overline{\mathrm{H_2O}}, \overline{T_a}, \overline{T_s})$. This equation is identical to equation (4a) but uses water vapor with fixed RH ($\mathrm{H_2O}^*$) from equation (6b). Next, the area exhibiting SGE is calculated with $\Delta\mathrm{OLR}_{\mathrm{FRH}}$ instead of ΔOLR in equation (7b). Table 8 shows that the area exhibiting SGE across Earth drastically reduces to 15% when using fixed RH compared to when varying RH is included (34%). Note that the value 34%, calculated using ERA+RRTM, agrees with the CERES EBAF's value of 36% (Table 7). In convective regions with large variations in RH, such as the Central Pacific, the areas exhibiting SGE with varying RH are 4 times as large as the areas with fixed RH alone.

Using equation (7b), we observe that the conditions for SGE are satisfied if $\Delta G > \Delta E$ and $\Delta T_s > 0$ or $\Delta G < \Delta E$ and $\Delta T_s < 0$. Thus, the surface emission, ΔE, serves as a threshold for the phenomenon. In Figure 7a we plot the time series of ΔG and ΔE over the Central Pacific using ERA-Interim data as input for RRTM. Throughout much of the time series, SGE conditions are satisfied with ΔG being outside the ΔE curve. This is particularly true during ENSO events (El Niño 2003, La Niña 2008, El Niño 2010, La Niña 2011–2012, El Niño 2015–2016), where ΔG significantly exceeds ΔE ($\Delta G \approx 2\Delta E$ in 2016). We decompose ΔG into its constituents: $\Delta G_{\mathrm{H_2O}}, \Delta G_{T_a}, and \quad \Delta G_{T_s}$. ΔG_{T_s} (solid purple) is always under the threshold line (dashed purple) because it is physically impossible for variations in surface temperature alone to push a region into an SGE state. The extra push to cross ΔE, overwhelmingly comes from the water vapor's contribution (orange), which faces only a small cancelation by ΔG_{T_a}.

Next, we break water vapor's radiative contributions into its altitude specific components over the Central Pacific (Figure 7e) as we did for the entire globe (Figure 2b). The middle tropospheric (green) water vapor traps the most radiation throughout the time series. We see that at the onset of an El Niño (e.g., 2009–2010 and 2015–2016) or a La Niña (e.g., 2007–2008 and 2010–2011), the middle troposphere traps much more radiation than other parts of the atmosphere for several months until the event reaches its peak, after which the upper troposphere efficiently contributes to $\Delta G_{\mathrm{H_2O}}$ due to deep convection. We explore why MT contributes the most to $\Delta G_{\mathrm{H_2O}}$ (Figures 7b–7d). The amount of infrared trapping by water vapor can be broken down into two components: the sensitivity, that is, Jacobian of $\Delta G_{\mathrm{H_2O}}$ to the water vapor mass anomaly ($\frac{\partial G}{\partial \mathrm{H_2O}}$ in units of W kg^{-1}) and the water vapor mass anomaly itself ($\Delta\mathrm{H_2O}$ in units of kg m^{-2}), that is, $\Delta G_{\mathrm{H_2O}} = \frac{\partial G}{\partial \mathrm{H_2O}} \times \Delta\mathrm{H_2O}$.

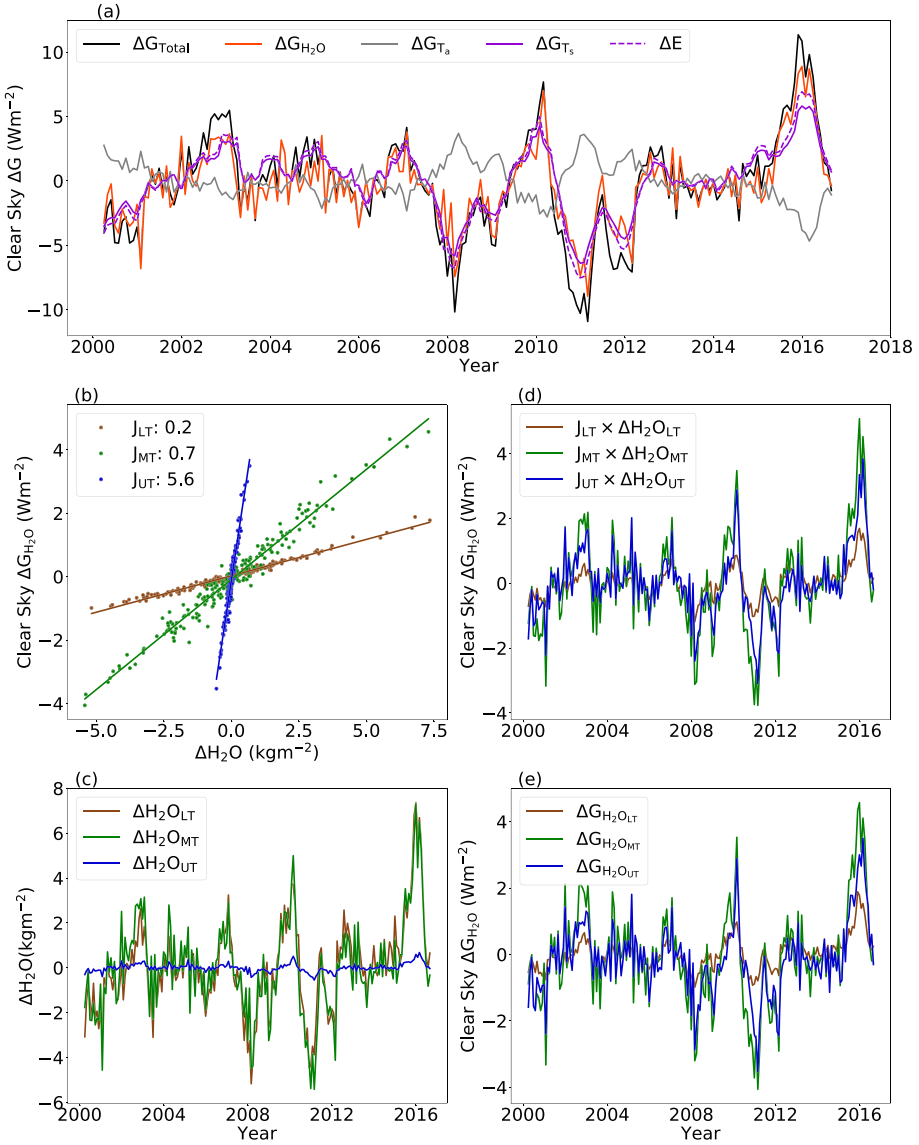

Figure 7. Clear sky greenhouse effect time series breakdown over the Central Pacific. (a) Components of ΔG_{Total} and how they interact to generate SGE (when ΔG_{Total} (black) is outside the ΔE threshold (dashed purple)). (b) Calculation of Jacobians: Sensitivity of water vapor greenhouse trapping to changes in water vapor mass in the lower, middle, and upper troposphere. (c) Mass of water vapor anomalies at altitudes mentioned in (b). (d) Multiplication of quantities in (b) and (c). (e) Radiative contributions by water vapor broken down by altitude.

First, we calculate the sensitivity in Figure 7b where we plot $\Delta G_{\text{H}_2\text{O}}$ due to the lower, middle, and upper troposphere against its respective water vapor anomalies. The slope from the linear regression gives us the sensitivity of $\Delta G_{\text{H}_2\text{O}}$ to $\Delta \text{H}_2\text{O}$. The upper troposphere (dark blue) has the largest sensitivity per a unit mass change in water vapor. It is followed by the middle troposphere (green) and then the lower troposphere (brown). Second, in Figure 7c we plot $\Delta \text{H}_2\text{O}$'s time series using ERA-I's input data. Although LT bears the majority of the column's mass, the anomalies in MT water vapor are of the same order of magnitude as the LT water vapor anomalies, if not slightly greater during some ENSO events. The UT anomalies in water vapor are an entire order of magnitude lower than that of LT and MT, as expected. Thus, when we multiply the sensitivity and the water vapor anomaly (Figure 7d) we obtain the water vapor greenhouse trapping due to the three parts of the troposphere. This shows that MT contributes the most to $\Delta G_{\text{H}_2\text{O}}$ because it sits in the "sweet spot" of intermediate sensitivity and $\Delta \text{H}_2\text{O}$ is the largest. Figure 7e shows that the above breakdown is identical to the ERA+RRTM anomalies. The moistening of the midtroposphere has contributed the most to the excess trapping of infrared radiation, rendering a super greenhouse effect.

4. Discussion

Our paper quantifies the origins of *G's* anomalies from March 2000 to August 2016, a longer time series than previous studies had used. We show that water vapor is a significant contributor to ΔG, locally and globally. Our paper and other studies (Dessler et al., 2008; Hallberg & Inamdar, 1993; Huang & Ramaswamy, 2008; Inamdar & Ramanathan, 1994; 1998) agree that water vapor in both the middle troposphere and upper troposphere is important in explaining the anomalous G in the deep tropics (Table 4). Our paper expands on this past work by demonstrating that water vapor in the middle and upper troposphere contribute nearly equally to ΔG even in the global mean and tropical mean (Figure 2b and Table 4). We further show that in smaller regions such as the West Pacific and Central Pacific, the midtroposphere's contributions exceed those of the upper troposphere's contributions.

Our study, however, arrives at different conclusions than the conclusions in Huang et al. (2007) and Stephens et al. (2016). In the tropics, during El Niño events, the middle troposphere and upper troposphere contribute equally to ΔG (Table 4). Focusing just on the 2015–2016 El Niño instead of looking at a composite of El Niño events, we find that the middle troposphere contributes more than the upper troposphere to ΔG for the tropics. This is in contrast to Huang et al. 2007 finding that water vapor in the upper troposphere contributes more than water vapor in the middle troposphere to ΔOLR, in the tropics during the 1998 El Niño. We find that in regions with high surface temperatures such as the West and Central Pacific, contributions from midtropospheric water vapor exceeds contributions from the rest of the column (Figure 7 and Table 4). This is in disagreement with Stephens et al., 2016's 2016 result that in regions of high surface temperature, upper tropospheric water vapor contributes more to OLR than the rest of the column's water vapor.

The different conclusions between our work and Huang et al. (2007) and Stephens et al. (2016) may be attributable to the following: (1) different definitions of the upper troposphere, (2) varying perturbation methods, (3) dissimilar El Niño events, and (4) the length of the time period considered. First, we define the upper troposphere as 400–150 hPa, whereas Huang et al. (2007) considers a deeper upper troposphere ranging from 400–100 hPa. Stephens et al. (2016) does not define the upper troposphere. A larger upper troposphere contains more water vapor and could contribute more to ΔG. Second, our PRP method computes monthly anomalies using a climatology from a long time series whereas both studies assumed a fixed perturbation of +10% moistening at each layer. Fixed perturbations may not be representative of observed anomalies, that is, deviations from a climatology. Third, we analyze different El Niño events. It may be that the 1998 El Niño moistened the upper troposphere more than the 2015–2016 El Niño and this yielded a larger contribution to ΔG. Fourth, our study considers the time period March 2000 to August 2016 whereas Huang et al. (2007) considered the 1989 La Niña and the 1998 El Niño in isolation. Stephens et al. (2016) used a climatology of the 2012 Atmospheric Infrared Sounder (AIRS) profiles. A longer time series contains more variance and results derived from it are less susceptible to noise as compared to short time periods of a single year.

Our paper shows that even in regions of low surface temperature, variations in RH can make a region exhibit the super greenhouse effect (Figure 6). We estimate that 46% of the tropics exhibit the SGE. Intriguingly, this is in agreement with an earlier study (Valero et al., 1997) that calculated the clear sky SGE only for regions above surface temperatures of 298 K, used ERBE's shorter data set from 1985 to 1989, and used the rate of change of G (equation (7b)) instead of anomalies (equation (7b)). They found the area that experienced SGE to be 52%.

It is interesting to consider the impact of clouds on the SGE. First, we consider the longwave radiative impact of clouds. This can be calculated using all-sky OLR from CERES EBAF 4.1 "t" in equation (7b). The area that exhibits SGE increases by 8% to 44%, globally. Regions that did not exhibit SGE under clear sky conditions, do exhibit SGE when clouds are included due to their longwave trapping effect. This has also been observed by Stephens et al. (2016) and Dewey and Goldblatt (2018). Second, we consider the shortwave radiative impact of clouds in addition to the longwave radiative impact. This redefines SGE in terms of the total radiation escaping to space. This is calculated using the sum of all-sky OLR and all-sky reflected shortwave radiation in equation (7b). We find that the area exhibiting SGE further increases by 8% to 52%, globally. This implies that even though clouds have a net cooling effect in the global mean, anomalies in the cloud radiative effect enhance the SGE.

Future studies may investigate the impact of decadal variability on G using a longer time series, explore the vertical breakdown of atmospheric temperature contributions, and probe the observed line-by-line spectral observations of OLR from AIRS to disentangle temperature and water vapor contributions to the clear sky greenhouse effect in the middle troposphere and upper troposphere as proposed by Huang and Ramaswamy (2008). These investigations would shed light on the water vapor and lapse rate feedbacks at high altitudes on decadal time scales, which could help refine estimates of transient climate response and climate sensitivity.

Acknowledgments
The authors would like to thank Nadir Jeevanjee, Yi Ming, and Leo Donner for reviewing an earlier version of this manuscript. We thank the three anonymous reviewers for helpful comments that greatly improved this manuscript. SP. Raghuraman was supported by the Cooperative Institute for Climate Science under Contract NA140AR4320106 . The authors declare no conflicts of interest. CERES EBAF Edition 4.1 data were obtained from the NASA Langley Research Center Atmospheric Science Data Center. Oceanic Nio Index data were obtained from NOAA's Climate Prediction Center (https://www.cpc.ncep.noaa.gov/). Data used in this study is available at ftp://data1.gfdl.noaa.gov/users/Shiv.Raghuraman/RaghuramanJGRA19/GFDL-AM4_ERA-I_CERES-EBAF/.

References

Andrews, T., Gregory, J. M., Webb, M. J., & Taylor, K. E. (2012). Forcing, feedbacks and climate sensitivity in CMIP5 coupled atmosphere-ocean climate models. *Geophysical Research Letters*, *39*, L09712. https://doi.org/10.1029/2012GL051607

Becker, T., & Stevens, B. (2014). Climate and climate sensitivity to changing CO_2 on an idealized land planet. *Journal of Advances in Modeling Earth Systems*, *6*, 1205–1223. https://doi.org/10.1002/2014MS000369

Briegleb, B. (1992). Longwave band model for thermal radiation in climate studies. *Journal of Geophysical Research*, *97*(D11), 11,475–11,485.

Colman, R. (2015). Climate radiative feedbacks and adjustments at the earth's surface. *Journal of Geophysical Research: Atmospheres*, *120*, 3173–3182. https://doi.org/10.1002/2014JD022896

Colman, R, Fraser, J, & Rotstayn, L (2001). Climate feedbacks in a general circulation model incorporating prognostic clouds. *Climate Dynamics*, *18*(1-2), 103–122.

Colman, R., & McAvaney, B. (2011). On tropospheric adjustment to forcing and climate feedbacks. *Climate dynamics*, *36*(9-10), 1649.

Dee, D. P., Uppala, S. M., Simmons, A., Berrisford, P., Poli, P., Kobayashi, S., et al. (2011). The ERA-Interim reanalysis: Configuration and performance of the data assimilation system. *Quarterly Journal of the royal meteorological society*, *137*(656), 553–597.

Dessler, A. (2013). Observations of climate feedbacks over 2000–10 and comparisons to climate models. *Journal of Climate*, *26*(1), 333–342.

Dessler, A., Yang, P, Lee, J, Solbrig, J, Zhang, Z, & Minschwaner, K (2008). An analysis of the dependence of clear-sky top-of-atmosphere outgoing longwave radiation on atmospheric temperature and water vapor. *Journal of Geophysical Research*, *113*, D17102. https://doi.org/10.1029/2008JD010137

Dessler, A., Zhang, Z, & Yang, P (2008). Water-vapor climate feedback inferred from climate fluctuations, 2003–2008. *Geophysical Research Letters*, *35*, L20704. https://doi.org/10.1029/2008GL035333

Dewey, M, & Goldblatt, C (2018). Evidence for radiative-convective bistability in tropical atmospheres. *Geophysical Research Letters*, *45*, 10,673–10,681. https://doi.org/10.1029/2018GL078903

Dudhia, A. (2017). The reference forward model (RFM). *Journal of Quantitative Spectroscopy and Radiative Transfer*, *186*, 243–253.

Gambacorta, A., Barnet, C., Soden, B., & Strow, L. (2008). An assessment of the tropical humidity-temperature covariance using airs. *Geophysical Research Letters*, *35*, L10814. https://doi.org/10.1029/2008GL033805

Hallberg, R., & Inamdar, A. K. (1993). Observations of seasonal variations in atmospheric greenhouse trapping and its enhancement at high sea surface temperature. *Journal of climate*, *6*(5), 920–931.

Held, I. M., & Soden, B. J. (2000). Water vapor feedback and global warming. *Annual review of energy and the environment*, *25*(1), 441–475.

Huang, Y. (2013). A simulated climatology of spectrally decomposed atmospheric infrared radiation. *Journal of Climate*, *26*(5), 1702–1715.

Huang, Y., & Ramaswamy, V (2008). Observed and simulated seasonal co-variations of outgoing longwave radiation spectrum and surface temperature. *Geophysical Research Letters*, *35*, L17803. https://doi.org/10.1029/2008GL034859

Huang, Y., Ramaswamy, V, & Soden, B. (2007). An investigation of the sensitivity of the clear-sky outgoing longwave radiation to atmospheric temperature and water vapor. *Journal of Geophysical Research*, *112*, D05104. https://doi.org/10.1029/2005JD006906

Inamdar, A., & Ramanathan, V. (1994). Physics of greenhouse effect and convection in warm oceans. *Journal of climate*, *7*(5), 715–731.

Inamdar, A. K., & Ramanathan, V. (1998). Tropical and global scale interactions among water vapor, atmospheric greenhouse effect, and surface temperature. *Journal of Geophysical Research*, *103*(D24), 32,177–32,194.

Kahn, B. H., Huang, X., Stephens, G. L., Collins, W. D., Feldman, D. R., Su, H., et al. (2016). ENSO regulation of far-and mid-infrared contributions to clear-sky olr. *Geophysical Research Letters*, *43*, 8751–8759. https://doi.org/10.1002/2016GL070263

Kato, S., Rose, F. G., Rutan, D. A., Thorsen, T. J., Loeb, N. G., Doelling, D. R., et al. (2018). Surface irradiances of edition 4.0 clouds and the earths radiant energy system (ceres) energy balanced and filled (ebaf) data product. *Journal of Climate*, *31*(11), 4501–4527.

Klocke, D., Quaas, J., & Stevens, B. (2013). Assessment of different metrics for physical climate feedbacks. *Climate dynamics*, *41*(5-6), 1173–1185.

Koll, D. D., & Cronin, T. W. (2018). Earths outgoing longwave radiation linear due to H_2O greenhouse effect. *Proceedings of the National Academy of Sciences*, *115*(41), 10,293–10,298.

Loeb, N. G., Doelling, D. R., Wang, H., Su, W., Nguyen, C., Corbett, J. G., et al. (2018). Clouds and the earths radiant energy system (CERES) energy balanced and filled (EBAF) top-of-atmosphere (toa) edition-4.0 data product. *Journal of Climate*, *31*(2), 895–918.

Manabe, S., & Wetherald, R. T. (1967). Thermal equilibrium of the atmosphere with a given distribution of relative humidity. *Journal of the Atmospheric Sciences*, *24*(3), 241–259.

Mlawer, E. J., Taubman, S. J., Brown, P. D., Iacono, M. J., & Clough, S. A. (1997). Radiative transfer for inhomogeneous atmospheres: RRTM, a validated correlated-k model for the longwave. *Journal of Geophysical Research*, *102*(D14), 16,663–16,682.

Otto, A., Otto, F. E., Boucher, O., Church, J., Hegerl, G., Forster, P. M., et al. (2013). Energy budget constraints on climate response. *Nature Geoscience*, *6*(6), 415.

Potter, G. L., Slingo, J. M., Morcrette, J.-J., & Corsetti, L. (1992). A modeling perspective on cloud radiative forcing. *Journal of Geophysical Research*, *97*(D18), 20,507–20,518.

Radley, C., Fueglistaler, S., & Donner, L. (2014). Cloud and radiative balance changes in response to ENSO in observations and models. *Journal of Climate*, *27*(9), 3100–3113.

Raschke, E, Kinne, S, & Stackhouse, P. (2012). Gewex radiative flux assessment (RFA), volume 1: Assessment, a project of the world climate research programme global energy and water cycle experiment (GEWEX) radiation panel (*WCRP Rep*).

Raval, A., & Ramanathan, V. (1989). Observational determination of the greenhouse effect. *Nature*, *342*(6251), 758.

Soden, B. J. (1997). Variations in the tropical greenhouse effect during El Niño. *Journal of climate*, *10*(5), 1050–1055.

Soden, B. J., & Fu, R. (1995). A satellite analysis of deep convection, upper-tropospheric humidity, and the greenhouse effect. *Journal of climate*, *8*(10), 2333–2351.

Stephens, G. L., Kahn, B. H., & Richardson, M. (2016). The super greenhouse effect in a changing climate. *Journal of Climate*, *29*(15), 5469–5482.

Trenberth, K. E. (1997). The definition of El Niño. *Bulletin of the American Meteorological Society*, *78*(12), 2771–2778.

Valero, F. P., Collins, W. D., Pilewskie, P., Bucholtz, A., & Flatau, P. J. (1997). Direct radiometric observations of the water vapor greenhouse effect over the equatorial Pacific Ocean. *Science*, *275*(5307), 1773–1776.

Wielicki, B. A., Wong, T., Allan, R. P., Slingo, A., Kiehl, J. T., Soden, B. J., et al. (2002). Evidence for large decadal variability in the tropical mean radiative energy budget. *Science*, *295*(5556), 841–844.

Wilber, A. C., Kratz, D. P., & Gupta, S. K. (1999). Surface emissivity maps for use in satellite retrievals of longwave radiation.

Wild, M., Hakuba, M. Z., Folini, D., Dörig-Ott, P., Schär, C., Kato, S., & Long, C. N. (2018). The cloud-free global energy balance and inferred cloud radiative effects: An assessment based on direct observations and climate models. *Climate Dynamics*, *52*, 1–26.

Zhao, M., Golaz, J-C, Held, I., Guo, H, Balaji, V, Benson, R, et al. (2018). The GFDL global atmosphere and land model am4. 0/lm4. 0: 1. Simulation characteristics with prescribed SSTs. *Journal of Advances in Modeling Earth Systems*, *10*, 691–734. https://doi.org/10.1002/2017MS001209